

# Effects of orbital selective dynamical correlation on the spin susceptibility and superconducting symmetries in $\text{Sr}_2\text{RuO}_4$

Chang-Youn Moon\*

*Advanced Instrumentation Institute,  
Korea Research Institute of Standards and Science,  
Yuseong, Daejeon 305-340, Republic of Korea*

(Dated: March 27, 2023)

## Abstract

We investigate the connection between the local electron correlation and the momentum dependence of the spin susceptibility and the superconducting gap functions in  $\text{Sr}_2\text{RuO}_4$ , using density-functional theory combined with dynamical mean-field theory. Adopting frequency-dependent two-particle vertex moves the zero energy spin susceptibility peaks towards the Brillouin zone center, compared with random-phase approximation which basically retains the peak positions closer to the Brillouin zone boundary as determined by the Fermi-surface nesting. We find that  $d_{xy}$  orbital plays a central role here via its enhanced correlation strength. Solving the linearized Eliashberg equation from this spin susceptibility, prime candidates of the superconducting gap symmetry are a  $s$ -wave, along with a nearly degenerate  $d$ -wave solution, all in spin singlet. Furthermore, another set of degenerate spin singlet gap functions emerges, odd with respect to  $k$ -point as well as orbital exchanges. We show that the stability of these gap functions are strongly dependent on the peak position of the spin susceptibility in the Brillouin zone.

PACS numbers:

Keywords:

$\text{Sr}_2\text{RuO}_4$  remains as one of most intriguing superconductors with the possibility of highly exotic and unconventional superconductivity, even after three decades since its discovery [1]. Noticing the analogy with superfluid  $^3\text{He}$ , earlier studies kindled discussions on the  $p_x + ip_y$  pairing [2–6]. This order parameter can be characterized by two essentially independent properties; the chirality, implying non-zero orbital magnetic moment, and the spin-triplet pairing. Spin-triplet pairing scenario, however, has been put into a serious question after recent spin susceptibility measurements using nuclear magnetic resonance (NMR) Knight shift [7, 8] and polarized neutron scattering [9]. They show that the susceptibility is suppressed below  $T_c$  more consistently with the spin-singlet pairing, overruling an earlier contradicting Knight shift measurement [10]. The chirality, or time-reversal symmetry breaking (TRSB) more generally, has been supported by a recent zero-field muon spin relaxation (ZF- $\mu\text{SR}$ ) measurement under uniaxial stress resulting in split superconducting and TRSB transitions [11], together with earlier works using ZF- $\mu\text{SR}$  [12] and non-zero Kerr rotation [13, 14]. Evidences of the two-component order parameter [15, 16] also have appeared, which can serve as a broader constraint on the nature of pairing in which the possibility of the chirality is included. Combinations among even parity order parameters of such as  $s$ ,  $d$ , and  $g$  symmetries are now generally considered plausible candidates.

The local electronic configuration near the Fermi energy ( $E_F$ ) comprises four electrons in  $t_{2g}$  levels split from empty  $e_g$  levels within Ru  $d$  states, and hence  $\text{Sr}_2\text{RuO}_4$  is a multi-orbital system where Hund’s coupling  $J_H$  plays a significant role in local Coulomb correlations. Consequently its normal-state behaviors, such as the crossover from high-temperature incoherent phase to low-temperature Fermi-liquid [2, 17–22] are understood in the context of Hund’s metals [23–26]. General features of Hund’s metals include strong local spin fluctuation and orbital differentiation [27, 28], as manifested in  $\text{Sr}_2\text{RuO}_4$  with much enhanced effective mass of  $d_{xy}$ -derived Fermi surface (FS) sheet compared with  $d_{xz/yz}$  derived ones [2, 23]. Then it is an important question that how the local correlation that governs the normal state works on the superconductivity. Assuming the spin-fluctuation-mediated superconductivity, the two-particle vertex, which forms fully interacting spin susceptibility ( $\chi$ ) when combined with the polarization bubble ( $\chi^0$ ), is one of major channels through which the local correlation effect is incorporated in electron pairing. While some of previous theoretical studies adopted the random-phase-approximation (RPA) for the vertex keeping the lowest order scattering process [29–34], others found that using frequency dependent vertex

produces qualitative differences in susceptibility and superconductivity [35–37]. However, distinctive roles played by the orbital selectivity and its dynamic nature in the susceptibility evaluation remain elusive especially with respect to the features critically connected to the pairing symmetry, such as the peak position of the susceptibility.

In this study, we demonstrate how the dynamic local correlations shape the susceptibility in the  $k$ -space and the pairing symmetry in  $\text{Sr}_2\text{RuO}_4$  within the framework of density-functional theory combined with dynamical mean-field theory (DFT+DMFT). Adopting the dynamic vertex results in the peak position of spin susceptibility closer to the Brillouin zone (BZ) center compared with RPA case, in better agreement with experimental measurements. We argue it originates from the stronger frequency dependence of the vertex within the  $d_{xy}$  orbital than the other  $t_{2g}$  components, relocating the peak off the position determined by simple FS nesting as in the RPA case. When the linearized-Eliashberg equation is constructed from the susceptibility and solved, the most probable gap function turns out to be of a  $s$ -wave symmetry with nodes followed by a  $d$ -wave solution slightly less stable, suggesting a possible two-component order parameter with an accidental degeneracy. Another plausible solutions are found to be symmetry-protected doubly degenerate ones which are odd with respect to both  $k$  and orbital exchanges. We show that the relative stability of these gap functions changes drastically between the respective susceptibility peak positions from the dynamical vertex and RPA, emphasizing on the importance of the accurate evaluation of the susceptibility in  $k$ -space and of the orbital selective and dynamic local correlation effects which enable it.

We use the modern implementation of DFT+DMFT method within all electron embedded DMFT approach [38] which is based on Wien2k [39], without downfolding or other approximations. The code is freely available on the web [40]. We employ LDA exchange-correlation functional [41, 42], and the quantum impurity model is solved by the continuous time quantum Monte Carlo (CTQMC) impurity solver [43]. Here sampled quantities are expanded in the basis function obtained by the singular value decomposition of the kernel for analytic continuation, ensuring reduced high-frequency noise [44]. Internal atomic positions are optimized, and  $U = 4.5$  eV and  $J = 1.0$  eV are adopted consistently with a previous study on this material [45] employing the same computational method. We use the Slater parametrization of the Coulomb interaction in this study, and our  $U$  and  $J$  parameters are defined with respect to the three Slater parameters in such a way that  $F^0 = U$ ,

$F^2 = 112/13 J$ , and  $F^4 = 70/13 J$ . BZ integration is done on the  $30 \times 30 \times 30$  k-point mesh for the body-centered tetragonal primitive unitcell in converging charge density and self energy, while  $40 \times 40 \times 2$  mesh in the BZ for the conventional tetragonal unitcell is used for the susceptibility and gap function calculations. All calculations are done in 116 K. Spin-orbit coupling (SOC) can have non-negligible effects on the electronic structure mainly near the region where different sheets of FS intersect, by strong orbital mixing [46–48]. As evaluating the two-particle vertex including SOC is still not available, and also considering susceptibilities are less affected by SOC than one-particle spectra [33], we neglect SOC in this work.

Figure 1(a) shows our calculated FS in the body-centered tetragonal BZ. Two one-dimensional (1D) FS sheets ( $\alpha$  and  $\beta$ ) are almost purely  $d_{xz}$  and  $d_{yz}$ -derived, respectively, while two-dimensional (2D) FS ( $\gamma$ ) is from  $d_{xy}$ , consistently with previous studies. All local correlation effects as contained in the dynamical self energy are included. Then we evaluated the susceptibility  $\chi$ , the polarization bubble  $\chi^0$ , and the two-particle vertex  $\Gamma$  which are related by the Bethe-Salpeter equation for a given bosonic Matsubara frequency  $\Omega$  *which is fixed to zero* in this work:  $\chi_{\alpha\alpha';\beta\beta'}^{s/c}(i\nu, i\nu', q) = ((\chi^0(q))^{-1} - \Gamma^{s/c})_{\alpha\alpha';\beta\beta'}^{-1}(i\nu, i\nu')$ . All the two-particle quantities are defined in the particle-hole channel if not explicitly indicated otherwise, and  $s/c$  stands for spin/charge.  $\Gamma^{s/c}$  is a dynamic local quantity containing all two-particle-irreducible diagrams and is obtained in the impurity solver [50, 51], as is the self energy which is the one-particle counterpart of the vertex. We display  $\Gamma^s \chi^s \Gamma^s \equiv [\Gamma \chi \Gamma]^s$ , which acts as an effective pairing potential in the Eliashberg equation, for the  $d_{xy}$  orbital channel at the lowest fermionic Matsubara frequency ( $i\nu = i\nu' \approx 0$ ) [52] in Fig. 1(b). There is a strong peak at  $q = (0.3, 0.3) \equiv Q_\omega$  where X point is at  $(0.5, 0.5)$ , reproducing the peak position of  $\chi$  from measurement [53] and previous calculation [36]. Note that  $[\Gamma \chi \Gamma]^s$  has basically the same peak structure with  $\chi^s$  in BZ, since the matrix multiplication between  $\Gamma^s$  and  $\chi^s$  corresponds to the weighted summation over different components of  $\chi^s$  which have similar momentum structure with one another. To highlight the effect of frequency dependence of the vertex, we evaluate  $[\Gamma \chi \Gamma]^s$  in Fig. 1(d) using the frequency-averaged (static) vertex corresponding to the equal-time component, which is equivalent to RPA. The peak is now at  $q = (0.35, 0.35) \equiv Q_{\text{RPA}}$  closer to X compared with  $Q_\omega$  also consistently with the previous calculation [36], suggesting that the momentum structure of the susceptibility alters with local correlations having different dynamic structures.  $d_{xz/yz}$  components have the

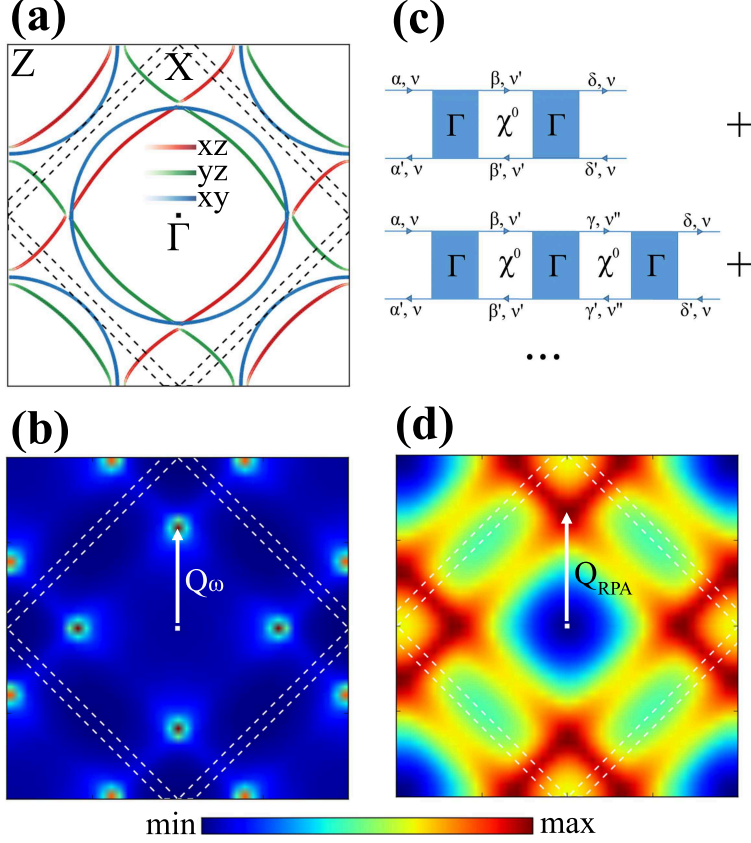


FIG. 1: (a) Fermi surface shown on the  $k_z = 0$  plane. Orbital character is denoted by the depth of the color as well as the thickness of the line. (b)  $[\Gamma\chi\Gamma]_{\alpha\alpha;\alpha\alpha}^s(i\nu, i\nu)$  where  $\alpha = d_{xy}$  and  $i\nu \approx 0$  on the  $k_z = 0$  plane. The momentum transfer of one of the four equivalent peaks inside the first Brillouin zone is marked by  $Q_\omega$ . (c) Infinite series expansion of  $[\Gamma\chi\Gamma]_{\alpha\alpha';\delta\delta'}^s(i\nu, i\nu)$  by the Bethe-Salpeter equation. Here the polarization bubble  $\chi^0$  is assumed to be diagonal in orbital indices (see the main text). (d) Same with (b) but using the frequency-averaged constant two-particle vertex instead of the dynamic vertex. The peak is denoted by  $Q_{\text{RPA}}$ .

same peak position with  $d_{xy}$ , but with a distinctively reduced amplitude, both for dynamic and static vertices [49] where the orbital selectivity is inscribed. The charge counterpart,  $[\Gamma\chi\Gamma]^c$ , is found to be negligible compared with  $[\Gamma\chi\Gamma]^s$  for the dynamic vertex, while they are comparable for the static vertex [49]. Now we are ready to reveal the mechanism of how the orbital selectivity encoded in the local vertex determines the peak position of the susceptibility in the  $k$ -space. To facilitate isolating the role of each orbital in its respective dynamic structure, we calculate  $[\Gamma\chi\Gamma]^s$  with inter-orbital components of the vertex turned off, i.e.,  $\Gamma_{\alpha\alpha';\beta\beta'}^s = \Gamma_{\alpha\alpha';\alpha\alpha'}^s \delta_{\alpha,\beta} \delta_{\alpha',\beta'}$ , and display it in Fig. 2. Since the FSs are almost com-

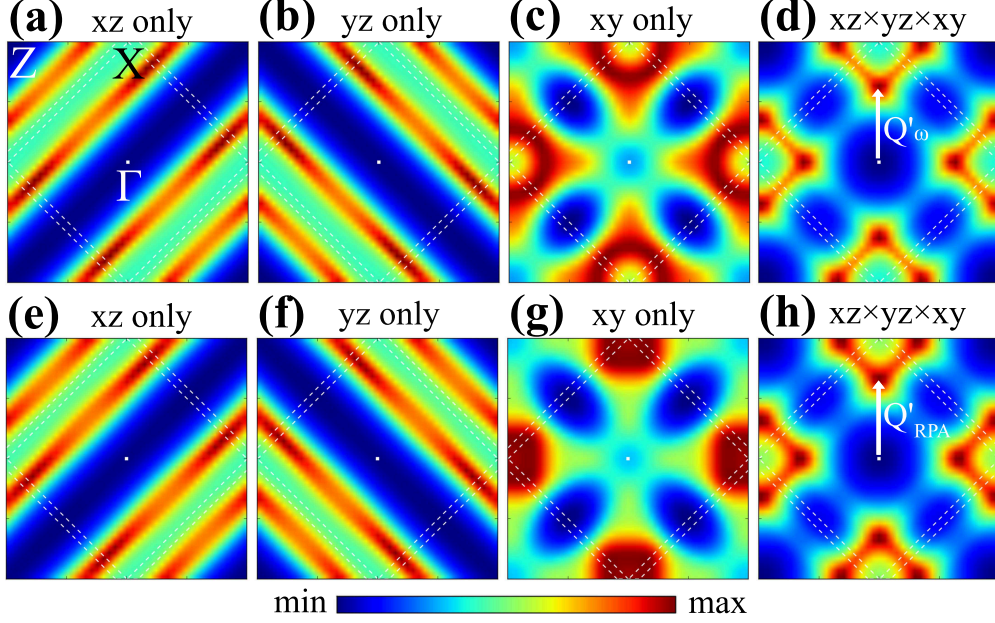


FIG. 2: With inter-orbital components of the vertex  $\Gamma$  set to zero,  $[\Gamma\chi\Gamma]_{\alpha\alpha;\alpha\alpha}^s(i\nu \approx 0, i\nu \approx 0)$  is calculated for  $\alpha = d_{xz/yz/xy}$  in (a)/(b)/(c). (e)/(f)/(g) is the same with (a)/(b)/(c), but using the frequency-averaged constant two-particle vertex instead of the dynamic vertex. (d) is obtained by multiplying (a), (b), and (c), while (h) is from multiplying (e), (f), and (g). The peak position is denoted by  $Q'_\omega/Q'_{\text{RPA}}$  in (d)/(h).

pletely decoupled in orbitals as seen in Fig. 1(a), the polarization bubble, defined as the product of two counter-propagating one-particle Green's functions, is also nearly diagonal:  $\chi_{\alpha\alpha';\beta\beta'}^0(q) \approx \chi_{\alpha\alpha';\beta\beta'}^0(q)\delta_{\alpha,\beta}\delta_{\alpha',\beta'} \equiv \chi_{\alpha\alpha'}^0(q)$ . Then  $[\Gamma\chi\Gamma]_{\alpha\alpha;\alpha\alpha}^s(i\nu, i\nu', q)$  is mostly composed of  $\chi_{\alpha\alpha}^0(i\nu'', q)$  with the weight of  $\Gamma_{\alpha\alpha;\alpha\alpha}^s(i\nu'', i\nu''')$  for the intermediate frequencies  $i\nu''$  and  $i\nu'''$ , but without incorporating orbital component other than  $\alpha$  in the infinite series as illustrated in Fig. 1(c). The diagonal component of  $[\Gamma\chi\Gamma]^s$  in  $d_{xz}$  orbital for  $i\nu = i\nu' \approx 0$  is shown in Fig. 2(a). The stripe pattern along the  $x$  direction is from the FS nesting in the  $d_{xz}$ -originated 1D FS sheet, and the same is true for the  $d_{yz}$  component displayed in Fig. 2(b) with  $\pi/2$  rotation. The fact that the  $k$ -dependence of  $[\Gamma\chi\Gamma]^s$  is determined by the simple FS nesting suggests that the vertex depends only weakly on the frequency, decoupling the polarization bubble from the vertex in the frequency domain for a given order of the infinite series in Fig. 1(c). Then the summation of the intermediate frequency produces  $\sum_\nu \chi^0(i\nu) = \chi^0(\Omega = 0)$ , the polarization bubble in zero bosonic frequency which is characterized by the FS nesting. Indeed, these results are almost identical with those from



frequency-averaged static vertex as displayed in Fig. 2(e) and Fig. 2(f). In case of the  $d_{xy}$  channel,  $[\Gamma\chi\Gamma]^s$  exhibits a four-fold rotation symmetry with weights around X points in the BZ reflecting the symmetry of the orbital as shown in both Fig. 2(c) and Fig. 2(g) for the dynamic and frequency-averaged static vertices, respectively. On the contrary to the  $d_{xz/yz}$  channels, however, there is a noticeable difference between the two vertices. Weights are distributed farther away from the  $\Gamma$  point for the dynamic vertex, which results from the frequency-dependent coefficient (i.e., vertex) of  $\chi^0(i\nu)$  in the frequency ( $\nu$ ) summation [49].

As the next step, orbital-separate contributions shown in Fig. 2(a)-(c)/(e)-(g) can be effectively coupled again to re-introduce inter-orbital components in  $[\Gamma\chi\Gamma]^s$ , by simply multiplying the contributions from each orbital channel. This is because inter-orbital terms consisting of the product among  $\chi^0$ 's with different orbital indices, such as  $\chi_{xy\ xy}^0\chi_{xz\ xz}^0$ , are restored by the multiplication in the infinite series expansion of  $[\Gamma\chi\Gamma]^s$  as displayed in Fig. 1(c). Figure 2(d)/(h) is obtained by multiplying Fig. 2(a)/(e), (b)/(f), and (c)/(g), and indeed reproduces the strong peak structure as seen in the original full vertex calculation result in Fig. 1(b)/(d) which includes both intra- and inter-orbital components. Moreover, the peak position from the dynamic vertex in Fig. 2(d) at  $Q'_\omega \approx (0.32, 0.32)$  is closer to the zone center than that from the static vertex at  $Q'_{\text{RPA}} \approx (0.35, 0.35)$ , also in accordance with the full vertex results. Having demonstrated that  $[\Gamma\chi\Gamma]^s$  can be effectively reconstructed from the product of orbital-separate components, it is evident that the difference of the peak position between by using the dynamic and static vertices mainly originates from the contrasting weight distributions of the  $d_{xy}$  contribution: weight is distributed closer to  $\Gamma/X$  point in Fig. 2(c)/(g), resulting in the peak closer to  $\Gamma/X$  point in Fig. 2(d)/(h). Therefore, we can conclude it is the  $d_{xy}$  component of the vertex that is responsible for the shift of the peak position from  $Q_{\text{RPA}} = (0.35, 0.35)$ , as determined by the FS nesting, to  $Q_\omega = (0.3, 0.3)$ , via its strong frequency dependence. This is true not only for  $\alpha = d_{xy}$  but also for  $\alpha = d_{xz/yz}$  in  $[\Gamma\chi\Gamma]_{\alpha\alpha;\alpha\alpha}^s$  [49] which also incorporates  $\chi_{xy\ xy}^0$  through the inter-orbital vertex. The pronounced dynamic nature of the  $d_{xy}$  component of the vertex is consistent with  $d_{xy}$  orbital's larger mass enhancement factor pointing to the larger correlation effect than  $d_{xz/yz}$ , which was suggested to originate from the proximity of the van Hove singularity of  $d_{xy}$  band to  $E_F$  [23].

Having calculated  $[\Gamma\chi\Gamma]^{s/c}$ , we can solve the linearized Eliashberg equation which also has been adopted in previous works [33, 34, 37, 54], derived from the divergence condition

of the susceptibility in the particle-particle channel:

$$-k_B T \sum_{k'\nu'\alpha'\beta'\gamma\delta} \Gamma_{\alpha\beta;\alpha'\beta'}^{pp,s/t}(k\nu; k'\nu') \chi_{\alpha'\beta'\gamma\delta}^{0,pp}(k'\nu') \Delta_{\gamma\delta}(k'\nu') = \lambda \Delta_{\alpha\beta}(k\nu)$$

where the eigenvalue  $\lambda$  and the eigenfunction  $\Delta$  can be interpreted as the pairing strength and the gap function, respectively.  $\Gamma^{pp,s/t}$  is the irreducible vertex in the particle-particle channel and consists of different combinations of  $[\Gamma\chi\Gamma]^{s/c}$  in interchanged momentum and orbital indices depending on spin singlet/triplet (s/t) pairing. Details of the formalism adopted in this study are found in Ref. [51]. Here we assume the constant frequency dependence of  $\Gamma^{pp}$  so that  $\Gamma^{pp}(i\nu, i\nu') = \Gamma^{pp}(i\nu \approx 0, i\nu' \approx 0)$ , then the resultant gap function  $\Delta(k)$  does not depend on the frequency either as in the BCS approximation where only even-frequency solutions can be captured. Nevertheless, it should be noted that the internal frequency summations are performed without any approximation which is found to be essential to obtain the correct peak position of  $[\Gamma\chi\Gamma]^s$  as demonstrated above. The gap function so obtained is distributed over entire BZ in the orbital basis and in principle at zero energy, and hence need to be projected to the FS where spectral function is to be evaluated at zero energy:

$$\Delta_{ij}(k) = \sum_{\alpha\beta, i'j'} \Psi_{k,ii'}^L U_{k,i'\alpha} \Delta_{\alpha\beta}(k) U_{k,\beta j'}^\dagger \Psi_{k,j'j}^R$$

. Here  $\Psi_{k,ii'}^{L/R}$  is the  $i$ th left/right eigenvector in  $i'$ th DFT band basis, of the complex DMFT eigenvalue equation at zero energy, and  $U_{k,i'\alpha}$  is the projector between orbital  $\alpha$  and  $i'$ th DFT band at  $k$  [38, 51]. This gives us more familiar gap functions similar with those defined in the band-based mean-field formalism instead of Green's functions. The gap functions for three largest eigenvalues are displayed in Fig. 3(a)-(c), all of which are in spin singlet. The most probable solution with  $\lambda = 0.0111$  is from the  $d_{xy}$  band and has a  $s$ -wave symmetry with nodes ("nodal  $s$ -wave",  $A_{1g}$  irreducible representation), followed by a slightly less stable solution ( $\lambda = 0.0101$ ) with also  $d_{xy}$  orbital character but in the  $d_{x^2-y^2}$  symmetry ( $B_{1g}$  irreducible representation). Besides the symmetry-imposed nodes at the intersections between 2D and 1D FS sheets where the gap function changes the sign, there are also regions with depleted weights around the van Hove point on the 2D FS for the  $d_{x^2-y^2}$  solution. The proximity of the eigenvalues or the accidental (near) degeneracy between the  $s$ - and  $d$ -wave solutions points to the possibility of the TRSB  $s + id$  order parameter suggested earlier [29–32], although it is  $s + id_{xy}$  rather than  $s + id_{x^2-y^2}$  that is more consistent with recent



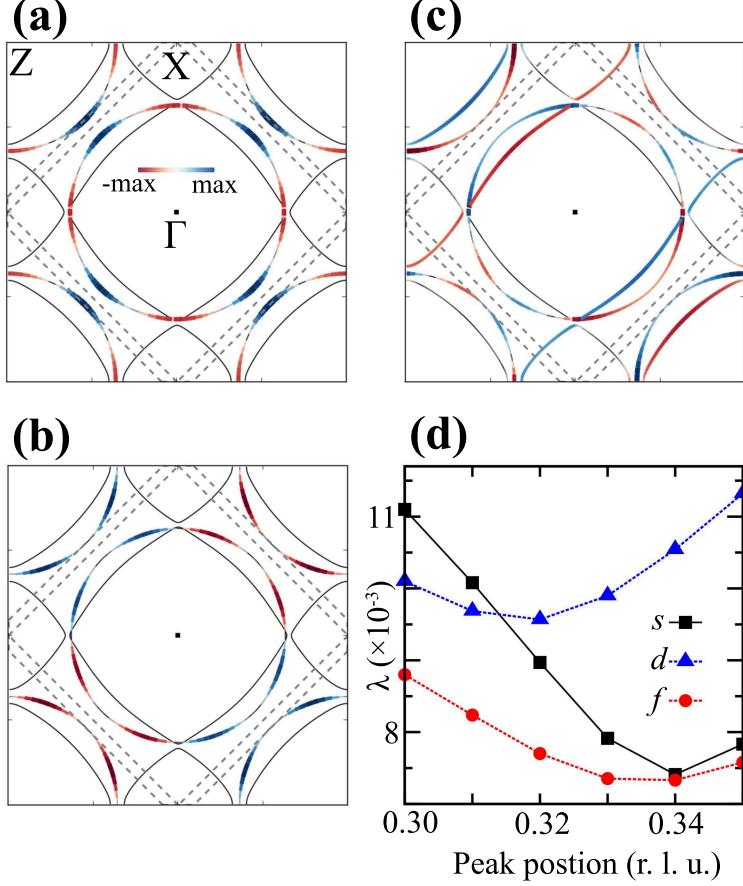


FIG. 3: Superconducting gap functions with three largest eigenvalues from the linearized Eliashberg equation, projected to the DMFT band basis on the FS, all in spin singlet. Gap functions in (a) and (b) are both from the  $d_{xy}$  orbital with  $\lambda = 0.0111$  and  $0.0101$ , and with  $s$ - and  $d$ -wave symmetries, respectively.  $\lambda = 0.0088$  solutions are doubly degenerate, where one has the inter-orbital gap function between  $d_{xz}$  and  $d_{xy}$  as shown in (c), and the other is between  $d_{yz}$  and  $d_{xy}$  with the gap function  $\pi/2$  rotated from (c). These degenerate gap functions have odd-orbital and odd-parity  $f$ -wave symmetry. (d) Eigenvalue of each gap symmetry as a function of the peak position  $(q, q)$  in the spin susceptibility from  $Q_\omega$  ( $q=0.30$ ) to  $Q_{\text{RPA}}$  ( $q=0.35$ ). The peak of the spin susceptibility in an arbitrary position is approximated by a gaussian function centered at the position. Eigenvalues are rescaled so that they match the values from the original full calculation at  $Q_\omega$ .

experiments [15, 16, 31]. Meanwhile, the third largest eigenvalue ( $\lambda = 0.0088$ ) is associated with doubly degenerate solutions which are protected by the lattice symmetry. Unlike  $s$ - and  $d$ -wave solutions which represent intra-orbital (band) pairings within the  $d_{xy}$  orbital, the gap functions are inter-orbital between  $d_{xy}$  and  $d_{xz/yz}$ . One can see that the sign of the gap

function is the opposite between  $d_{xy}$  and  $d_{xz}$  FSs where they meet as in Fig. 3(c), indicating it is odd with respect to the orbital (band) interchange. Moreover, it is also odd in  $k$ -space ( $f$ -wave,  $E_u$  irreducible representation), satisfying the antisymmetric fermion exchange rule :  $\hat{S}\hat{P}\hat{O}\hat{T} = -1 \times -1 \times -1 \times 1 = -1$ . Odd-parity pairing, usually combined with spin-triplet, here associates with spin-singlet which is only possible with the extra degree of freedom of orbitals, and hence is characteristic of the multi-orbital superconductivity. The degenerate pair of gap functions, one from  $d_{xy}$  and  $d_{xz}$  and another from  $d_{xy}$  and  $d_{yz}$  (Fig. 3(c) and its  $\pi/2$  rotation, respectively), can form a TRSB chiral order parameter  $f + if$ .

Our  $s$ -wave solution changes sign at every  $\pi/4$ , hence is effectively stabilized by the repulsive pairing potential peaked at the smaller momentum transfer  $Q_\omega$ , compared with longer  $Q_{\text{RPA}}$  determined by the FS nesting.  $Q_\omega$  is rather short to connect the van Hove regions having higher density of states, hence these regions are depleted in weight for the  $d$ -wave gap making it a relatively less stable solution. Indeed, Mazin *et al.* adopted susceptibility with a nesting-induced peak at  $Q \approx (1/3, 1/3)$  to obtain a  $d$ -wave gap with maximum weights at the van Hove point in their early work [55], while an  $s$ -wave gap has been suggested by using the peak position determined by inelastic neutron scattering at  $Q \approx (0.3, 0.3)$  [53] consistently with our result. To explicitly study the relative stability of each solution with respect to the susceptibility peak position, we employ the spin susceptibility  $([\Gamma\chi\Gamma]^s)$  consisting of simple gaussian peaks at any desired position in the BZ which should be a reasonable approximation seeing the simple peak structures of the original spin susceptibility shown in Fig. 1(b). Solving the gap equation from this susceptibility consisting of gaussian peaks, we display the result in Fig. 3(d). For  $s$ - and  $d$ -wave solutions, we adopt  $[\Gamma\chi\Gamma]^s$  with only  $d_{xy}$  diagonal component, while for the  $f$ -wave gap only the inter-orbital components between  $d_{xy}$  and  $d_{xz/yz}$  are set non-zero. The eigenvalue  $\lambda$  of each solution as a function of the peak position is rescaled so that it retains its original value from the full calculation at  $Q_\omega$ . As expected, the  $s$ -wave gap grows unstable with increasing momentum transfer, while the  $d$ -wave gap is more stable at  $Q_{\text{RPA}}$ . The stability of the  $f$ -wave gap also decreases from  $Q_\omega$  to  $Q_{\text{RPA}}$ , so that the  $d$ -wave is dominant over other gap symmetries at  $Q_{\text{RPA}}$ . Therefore, we can conclude that TRSB  $s + id$  and chiral  $f + if$  gap symmetries are stabilized by the antiferromagnetic spin fluctuation near  $Q_\omega = (0.3, 0.3)$ , which is only available by using the dynamical vertex function.

Low energy excitations and the presence of (vertical line) gap nodes are another require-

ment for the feasible gap symmetries imposed by experiments [56–61]. Our  $s$ - and  $d$ -wave solutions are from the  $d_{xy}$  FS, so the 1D FSs from  $d_{xz/yz}$  are basically gapless for each of the two solutions (see Fig. 3(a) and (b)) and also for their TRSB complex combination  $s + id$ . When SOC is included, the  $d_{xy}$  component would be incorporated on the 1D FSs due to the orbital mixing, but it is likely that some part of 1D FSs are still gapless. On the other hand, the condition for the existence of gap nodes is tighter for the chiral  $f + if$  order parameter, since both 2D and 1D FSs participate in this inter-orbital electron pairing (Fig. 3(c) and its  $\pi/2$  rotation). Nevertheless, the van Hove points in the 2D FS would have the least weight in the complex combination between a sign-changing node and the relatively smaller weight on the  $\pi/2$  rotated point. Further studies might be required to elaborate on the compatibility of our suggested gap symmetries with experimental observations, as well as the possible effect of SOC [34, 37].

In conclusion, we investigate the role of the dynamic local correlation in the spin susceptibility and the superconducting symmetry in  $\text{Sr}_2\text{RuO}_4$  within the DFT+DMFT framework. The two-particle vertex is found to weakly depend on the frequency within  $d_{xz/yz}$  orbitals while its  $d_{xy}$  component is strongly frequency-dependent, locating the peak of the spin susceptibility closer to the BZ center compared with the FS nesting-driven peak position. We find that the relatively smaller momentum transfer in the spin susceptibility stabilizes a  $s$ -wave gap with many sign-changing nodes while it is against the stability of the  $d$ -wave, resulting in an accidental near degeneracy of the two gap symmetries both in spin singlet. Odd-parity and odd-orbital  $f$ -wave spin singlet gap functions are also found with symmetry-protected double degeneracy, which can lead to the realization of a chiral superconductivity. Our work demonstrates how the local correlation and orbital selectivity in a Hund’s metal affect the non-local electronic structure in the two-particle level and the superconductivity.

The author thanks Y. Bang, I. I. Mazin, E.-G. Moon, and K. Haule for helpful discussions.

---

\* Electronic address: cymoon@kriss.re.kr

- [1] Y. Maeno, H. Hashimoto, K. Yoshida, S. Nishizaki, T. Fujita, J. G. Bednorz, and F. Lichtenberg, Superconductivity in a layered perovskite without copper, *Nature (London)* **372**, 532 (1994).

- [2] A. P. Mackenzie and Y. Maeno, The superconductivity of  $\text{Sr}_2\text{RuO}_4$  and the physics of spin-triplet pairing, *Rev. Mod. Phys.* **75**, 657 (2003).
- [3] T. M. Rice and M. Sigrist,  $\text{Sr}_2\text{RuO}_4$ : an electronic analogue of  $^3\text{He}$ ?, *J. Phys. Condens. Matter* **7**, L643 (1995).
- [4] M. Sigrist, Ehrenfest Relations for Ultrasound Absorption in  $\text{Sr}_2\text{RuO}_4$ , *Prog. Theor. Phys.* **107**, 917 (2002).
- [5] Y. Maeno, S. Kittaka, T. Nomura, S. Yonezawa, and K. Ishida, Evaluation of Spin-Triplet Superconductivity in  $\text{Sr}_2\text{RuO}_4$ , *J. Phys. Soc. Jpn.* **81**, 011009 (2012).
- [6] C. Kallin, Chiral p-wave order in  $\text{Sr}_2\text{RuO}_4$ , *Rep. Prog. Phys.* **75**, 042501 (2012).
- [7] A. Pustogow, Y. Luo, A. Chronister, Y. S. Su, D. A. Sokolov, F. Jerzembeck, A. P. Mackenzie, C. W. Hicks, N. Kikugawa, S. Raghu, E. D. Bauer, and S. E. Brown, Constraints on the superconducting order parameter in  $\text{Sr}_2\text{RuO}_4$  from oxygen-17 nuclear magnetic resonance, *Nature (London)* **574**, 72 (2019).
- [8] K. Ishida, M. Manago, K. Kinjo, and Y. Maeno, Reduction of the  $^{17}\text{O}$  Knight Shift in the Superconducting State and the Heat-up Effect by NMR Pulses on  $\text{Sr}_2\text{RuO}_4$ , *J. Phys. Soc. Jpn.* **89**, 034712 (2020).
- [9] A. N. Petsch, M. Zhu, M. Enderle, Z. Q. Mao, Y. Maeno, I. I. Mazin, and S. M. Hayden, Reduction of the Spin Susceptibility in the Superconducting State of  $\text{Sr}_2\text{RuO}_4$  Observed by Polarized Neutron Scattering, *Phys. Rev. Lett.* **125**, 217004 (2020).
- [10] K. Ishida, H. Mukuda, Y. Kitaoka, K. Asayama, Z. Q. Mao, Y. Mori, and Y. Maeno, Spin-triplet superconductivity in  $\text{Sr}_2\text{RuO}_4$  identified by  $^{17}\text{O}$  Knight shift, *Nature (London)* **396**, 658 (1998).
- [11] V. Grinenko, S. Ghosh, R. Sarkar, J.-C. Orain, A. Nikitin, M. Elender, D. Das, Z. Guguchia, F. Bruckner, M. E. Barber, J. Park, N. Kikugawa, D. A. Sokolov, J. S. Bobowski, T. Miyoshi, Y. Maeno, A. P. Mackenzie, H. Luetkens, C. W. Hicks, and H.-H. Klauss, Split superconducting and time-reversal symmetry-breaking transitions in  $\text{Sr}_2\text{RuO}_4$  under stress, *Nat. Phys.* **17**, 748 (2021).
- [12] G. M. Luke, Y. Fudamoto, K. M. Kojima, M. I. Larkin, J. Merrin, B. Nachumi, Y. J. Uemura, Y. Maeno, Z. Q. Mao, Y. Mori, H. Nakamura, and M. Sigrist, Time-reversal symmetry-breaking superconductivity in  $\text{Sr}_2\text{RuO}_4$ , *Nature (London)* **394**, 558 (1998).
- [13] J. Xia, Y. Maeno, P. T. Beyersdorf, M. M. Fejer, and A. Kapitulnik, High Resolution Polar

- Kerr Effect Measurements of  $\text{Sr}_2\text{RuO}_4$ : Evidence for Broken Time-Reversal Symmetry in the Superconducting State, *Phys. Rev. Lett.* **97**, 167002 (2006).
- [14] A. Kapitulnik, J. Xia, E. Schemm, and A. Palevski, Polar Kerr effect as probe for time-reversal symmetry breaking in unconventional superconductors, *New J. Phys.* **11**, 055060 (2009).
- [15] S. Benhabib, C. Lupien, I. Paul, L. Berges, M. Dion, M. Nardone, A. Zitouni, Z. Q. Mao, Y. Maeno, A. Georges, L. Taillefer, and C. Proust, Ultrasound evidence for a two-component superconducting order parameter in  $\text{Sr}_2\text{RuO}_4$ , *Nat. Phys.* **17**, 194 (2021).
- [16] S. Ghosh, A. Shekhter, F. Jerzembeck, N. Kikugawa, D. A. Sokolov, M. Brando, A. P. Mackenzie, C. W. Hicks, and B. J. Ramshaw, Thermodynamic evidence for a two-component superconducting order parameter in  $\text{Sr}_2\text{RuO}_4$ , *Nat. Phys.* **17**, 199 (2021).
- [17] T. Katsufuji, M. Kasai, and Y. Tokura, In-Plane and Out-of-Plane Optical Spectra of  $\text{Sr}_2\text{RuO}_4$ , *Phys. Rev. Lett.* **76**, 126 (1996).
- [18] T. Imai, A. W. Hunt, K. R. Thurber, and F. C. Chou,  $^{17}\text{O}$  NMR Evidence for Orbital Dependent Ferromagnetic Correlations in  $\text{Sr}_2\text{RuO}_4$ , *Phys. Rev. Lett.* **81**, 3006 (1998).
- [19] N. E. Hussey, A. P. Mackenzie, J. R. Cooper, Y. Maeno, S. Nishizaki, and T. Fujita, Normal-state magnetoresistance of  $\text{Sr}_2\text{RuO}_4$ , *Phys. Rev. B* **57**, 5505 (1998).
- [20] T. Valla, P. D. Johnson, Z. Yusof, B. Wells, Q. Li, S. M. Loureiro, R. J. Cava, M. Mikami, Y. Mori, M. Yoshimura, and T. Sasaki, Coherence–incoherence and dimensional crossover in layered strongly correlated metals, *Nature (London)* **417**, 627 (2002).
- [21] S.-C. Wang, H.-B. Yang, A. K. P. Sekharan, H. Ding, J. R. Engelbrecht, X. Dai, Z. Wang, A. Kaminski, T. Valla, T. Kidd, A. V. Fedorov, and P. D. Johnson, Quasiparticle Line Shape of  $\text{Sr}_2\text{RuO}_4$  and Its Relation to Anisotropic Transport, *Phys. Rev. Lett.* **92**, 137002 (2004).
- [22] T. E. Kidd, T. Valla, A. V. Fedorov, P. D. Johnson, R. J. Cava, and M. K. Haas, Orbital Dependence of the Fermi Liquid State in  $\text{Sr}_2\text{RuO}_4$ , *Phys. Rev. Lett.* **94**, 107003 (2005).
- [23] J. Mravlje, M. Aichhorn, T. Miyake, K. Haule, G. Kotliar, and A. Georges, Coherence–Incoherence Crossover and the Mass-Renormalization Puzzles in  $\text{Sr}_2\text{RuO}_4$ , *Phys. Rev. Lett.* **106**, 096401 (2011).
- [24] L. de’ Medici, J. Mravlje, and A. Georges, Janus-Faced Influence of Hund’s Rule Coupling in Strongly Correlated Materials, *Phys. Rev. Lett.* **107**, 256401 (2011).
- [25] J. Mravlje and A. Georges, Thermopower and Entropy: Lessons from  $\text{Sr}_2\text{RuO}_4$ , *Phys. Rev. Lett.* **117**, 036401 (2016).

- [26] F. B. Kugler, M. Zingl, H. U. R. Strand, S.-S. B. Lee, J. von Delft, and A. Georges, Strongly Correlated Materials from a Numerical Renormalization Group Perspective: How the Fermi-Liquid State of  $\text{Sr}_2\text{RuO}_4$  Emerges, *Phys. Rev. Lett.* **124**, 016401 (2020).
- [27] K. Haule and G. Kotliar, Coherence–incoherence crossover in the normal state of iron oxynictides and importance of Hund’s rule coupling, *New J. Phys.* **11**, 025021 (2009).
- [28] C.-Y. Moon, Strong enhancement of magnetic order from bulk to stretched monolayer FeSe as Hund’s metals, *npj Comput. Mater.* **6**, 147 (2020).
- [29] A. T. Romer, D. D. Scherer, I. M. Eremin, P. J. Hirschfeld, and B. M. Andersen, Knight Shift and Leading Superconducting Instability from Spin Fluctuations in  $\text{Sr}_2\text{RuO}_4$ , *Phys. Rev. Lett.* **123**, 247001 (2019).
- [30] A. T. Romer, A. Kreisel, M. A. Muller, P. J. Hirschfeld, I. M. Eremin, and B. M. Andersen, Theory of strain-induced magnetic order and splitting of  $T_c$  and  $T_{\text{TRSB}}$  in  $\text{Sr}_2\text{RuO}_4$ , *Phys. Rev. B* **102**, 054506 (2020).
- [31] A. T. Romer, P. J. Hirschfeld, and B. M. Andersen, Superconducting state of  $\text{Sr}_2\text{RuO}_4$  in the presence of longer-range Coulomb interactions *Phys. Rev. B* **104**, 064507 (2021).
- [32] A. T. Romer, T. A. Maier, A. Kreisel, P. J. Hirschfeld, and B. M. Andersen, Leading superconducting instabilities in three-dimensional models for  $\text{Sr}_2\text{RuO}_4$ , *Phys. Rev. Res.* **4**, 033011 (2022).
- [33] O. Gingras, R. Nourafkan, A.-M. S. Tremblay, and M. Cote, Superconducting Symmetries of  $\text{Sr}_2\text{RuO}_4$  from First-Principles Electronic Structure, *Phys. Rev. Lett.* **123**, 217005 (2019).
- [34] O. Gingras, N. Allaglo, R. Nourafkan, M. Cote, and A.-M. S. Tremblay, Superconductivity in correlated multiorbital systems with spin-orbit coupling: Coexistence of even- and odd-frequency pairing, and the case of  $\text{Sr}_2\text{RuO}_4$ , *Phys. Rev. B* **106**, 064513 (2022).
- [35] L. Boehnke, P. Werner, and F. Lechermann, Multi-orbital nature of the spin fluctuations in  $\text{Sr}_2\text{RuO}_4$ , *Euro Phys. Lett.* **122**, 57001 (2018).
- [36] H. U. R. Strand, M. Zingl, N. Wentzell, O. Parcollet, and A. Georges, Magnetic response of  $\text{Sr}_2\text{RuO}_4$ : Quasi-local spin fluctuations due to Hund’s coupling, *Phys. Rev. B* **100**, 125120 (2019).
- [37] S. Kaser, H. U. R. Strand, N. Wentzell, A. Georges, O. Parcollet, and P. Hansmann, Interorbital singlet pairing in  $\text{Sr}_2\text{RuO}_4$ : A Hund’s superconductor, *Phys. Rev. B* **105**, 155101 (2022).



- [38] K. Haule, C.-H. Yee, and K. Kim, Dynamical mean-field theory within the full-potential methods: Electronic structure of CeIrIn<sub>5</sub>, CeCoIn<sub>5</sub>, and CeRhIn<sub>5</sub>, *Phys. Rev. B* **81**, 195107 (2010).
- [39] P. Blaha, K. Schwarz, G. Madsen, D. Kvasnicka, and J. Luitz, WIEN2k (Vienna University of Technology, Vienna, 2001).
- [40] <http://hauleweb.rutgers.edu/tutorials/>.
- [41] D. M. Ceperley, and B. J. Alder, Ground State of the Electron Gas by a Stochastic Method, *Phys. Rev. Lett.* **45**, 566 (1980).
- [42] J. P. Perdew, and Y. Wang, Accurate and simple analytic representation of the electron-gas correlation energy, *Phys. Rev. B* **45**, 13244 (1992).
- [43] K. Haule, Quantum Monte Carlo impurity solver for cluster dynamical mean-field theory and electronic structure calculations with adjustable cluster base, *Phys. Rev. B* **75**, 155113 (2007).
- [44] H. Shinaoka, J. Otsuki, K. Haule, M. Wallerberger, E. Gull, K. Yoshimi, and M. Ohzeki, Overcomplete compact representation of two-particle Green's functions, *Phys. Rev. B* **97**, 205111 (2018).
- [45] X. Deng, K. Haule, and G. Kotliar, Transport Properties of Metallic Ruthenates: A DFT+DMFT Investigation, *Phys. Rev. Lett.* **116**, 256401 (2016). For detailed information on the Coulomb parametrization employed in this work, refer to <http://hauleweb.rutgers.edu/tutorials/CoulombUexplain.html>.
- [46] G. Zhang, E. Gorelov, E. Sarvestani, and Eva Pavarini, Fermi Surface of Sr<sub>2</sub>RuO<sub>4</sub>: Spin-Orbit and Anisotropic Coulomb Interaction Effects, *Phys. Rev. Lett.* **116**, 106402 (2016).
- [47] M. Kim, J. Mravlje, M. Ferrero, O. Parcollet, and A. Georges, Spin-Orbit Coupling and Electronic Correlations in Sr<sub>2</sub>RuO<sub>4</sub>, *Phys. Rev. Lett.* **120**, 126401 (2018).
- [48] A. Tamai, M. Zingl, E. Rozbicki, E. Cappelli, S. Ricco, A. de la Torre, S. McKeown Walker, F. Y. Bruno, P. D. C. King, W. Meevasana, M. Shi, M. Radovi, N. C. Plumb, A. S. Gibbs, A. P. Mackenzie, C. Berthod, H. U. R. Strand, M. Kim, A. Georges, and F. Baumberger, High-Resolution Photoemission on Sr<sub>2</sub>RuO<sub>4</sub> Reveals Correlation-Enhanced Effective Spin-Orbit Coupling and Dominantly Local Self-Energies, *Phys. Rev. X* **9**, 021048 (2019).
- [49] See Supplemental Material at [] for an extended discussion on the orbital, spin/charge, and vertex dependence of the susceptibility in the context of Hund's metals. Also included is a demonstration of the mechanism of the large difference in the spin susceptibility between using

dynamic and static vertices when only  $d_{xy}$ -orbital channel is allowed.

- [50] H. Park, K. Haule, and G. Kotliar, Magnetic Excitation Spectra in  $\text{BaFe}_2\text{As}_2$ : A Two-Particle Approach within a Combination of the Density Functional Theory and the Dynamical Mean-Field Theory Method, *Phys. Rev. Lett.* **107**, 137007 (2011).
- [51] Z. P. Yin, K. Haule, and G. Kotliar, Spin dynamics and orbital-antiphase pairing symmetry in iron-based superconductors, *Nat. Phys.* **10**, 845 (2014).
- [52] Because of the slight difference between the value at  $i\nu = i\nu' = 0^\pm$  and that at  $i\nu = -i\nu' = 0^\pm$ , where  $0^{+/-}$  represents the first positive/negative fermionic Matsubara frequency, we take the average between the two values. Same is true throughout this paper whenever this notation appears.
- [53] P. Steffens, Y. Sidis, J. Kulda, Z. Q. Mao, Y. Maeno, I.I. Mazin, and M. Braden, Spin Fluctuations in  $\text{Sr}_2\text{RuO}_4$  from Polarized Neutron Scattering: Implications for Superconductivity, *Phys. Rev. Lett.* **122**, 047004 (2019).
- [54] S. Acharya, D. Pashov, C. Weber, H. Park, L. Sponza, and M. V. Schilfgaarde, Evening out the spin and charge parity to increase  $T_c$  in  $\text{Sr}_2\text{RuO}_4$ , *Commun. Phys.* **2**, 163 (2019).
- [55] I. I. Mazin and D. J. Singh, Competitions in Layered Ruthenates: Ferromagnetism versus Antiferromagnetism and Triplet versus Singlet Pairing, *Phys. Rev. Lett.* **82**, 4324 (1999).
- [56] I. Bonalde, B. D. Yanoff, M. B. Salamon, D. J. Van Harlingen, E. M. E. Chia, Z. Q. Mao, and Y. Maeno, Temperature Dependence of the Penetration Depth in  $\text{Sr}_2\text{RuO}_4$ : Evidence for Nodes in the Gap Function, *Phys. Rev. Lett.* **85**, 4775 (2000).
- [57] K. Izawa, H. Takahashi, H. Yamaguchi, Y. Matsuda, M. Suzuki, T. Sasaki, T. Fukase, Y. Yoshida, R. Settai, and Y. Onuki, Superconducting Gap Structure of Spin-Triplet Superconductor  $\text{Sr}_2\text{RuO}_4$  Studied by Thermal Conductivity, *Phys. Rev. Lett.* **86**, 2653 (2001).
- [58] I. A. Firmo, S. Lederer, C. Lupien, A. P. Mackenzie, J. C. Davis, and S. A. Kivelson, Evidence from tunneling spectroscopy for a quasi-one-dimensional origin of superconductivity in  $\text{Sr}_2\text{RuO}_4$ , *Phys. Rev. B* **88**, 134521 (2013).
- [59] E. Hassinger, P. Bourgeois-Hope, H. Taniguchi, S. Rene de Cotret, G. Grissonnanche, M. S. Anwar, Y. Maeno, N. Doiron-Leyraud, and L. Taillefer, Vertical Line Nodes in the Superconducting Gap Structure of  $\text{Sr}_2\text{RuO}_4$ , *Phys. Rev. X* **7**, 011032 (2017).
- [60] S. Kittaka, S. Nakamura, T. Sakakibara, N. Kikugawa, T. Terashima, S. Uji, D. A. Sokolov, A. P. Mackenzie, K. Irie, Y. Tsutsumi *et al.*, Searching for Gap Zeros in  $\text{Sr}_2\text{RuO}_4$  via Field-

- Angle-Dependent Specific-Heat Measurement, *J. Phys. Soc. Jpn.* **87**, 093703 (2018).
- [61] R. Sharma, S. D. Edkins, Z. Wang, A. Kostin, C. Sow, Y. Maeno, A. P. Mackenzie, J. C. S. Davis, and V. Madhavan, Momentum-resolved superconducting energy gaps of  $\text{Sr}_2\text{RuO}_4$  from quasiparticle interference imaging, *Proc. Natl. Acad. Sci. USA* **117**, 5222 (2020).